Elucidating cloud vertical structures based on three-year Ka-band cloud radar observations from Beijing, China

Yong Zhang[a], Qing Zhou[a], Shanshan Lv[a], Shuze Jia[b], Fa Tao[a], Dandan Chen[c], Jianping Guo[c],*

[a] Meteorological Observation Center, China Meteorological Administration, Beijing 100081, China
[b] National Satellite Meteorological Center, China Meteorological Administration, Beijing 100081, China
[c] State Key Laboratory of Severe Weather, Chinese Academy of Meteorological Sciences, Beijing 100081, China

ABSTRACT

Elucidating the vertical structures of clouds is key to reducing the uncertainty in cloud-induced climate forcing; however, we do not yet know explicitly about the cloud structures that form over Beijing, China, and how they vary. In this paper, we document vertically resolved cloud structures and their climatological variation based on three-year (1 January 2015 to 31 December 2017) ground-based Ka-band (35 GHz) millimeter-wave cloud radar (MMCR) measurements. Cloud top height (CTH) and radar reflectivity are higher in summer and autumn than in spring and winter. We verified the MMCR measurements of the CTH and cloud base height (CBH) independently based on observations from the Himawari-8 and CL51 ceilometer at the same station, respectively. The CTH decreased as the thickness of the cloud layer increased. This may have been due to the mechanism used to determine the CTH, which was based on data from the satellite infrared channel. There were two peaks in the CBH distribution, located at 0–1 km and 5–6 km, whereas the frequency of the CTH peaked at an altitude of 9–10 km, between 1200 and 1800 LST. Precipitating clouds tended to be located at lower altitudes and exhibited stronger radar reflectivities than non-precipitating clouds. The cloud frequency tended to peak in autumn and reached a minimum in winter. In terms of the seasonality of clouds at various levels, middle- and high-level clouds were dominant over Beijing, with high and low (precipitating) clouds concentrated between May and October. Mid-altitude clouds occurred more frequently in winter and spring. CTH peaked in summer due to the strong solar radiation received by the surface. In contrast, minimum CBH occurred in winter. The cloud heights were higher and radar reflectivities larger than reported in previous studies. These results are correlated with urban warming effects. Understanding the properties of clouds will not only be of benefit to researchers carrying out cloud forcing studies, but will also provide key validation data for climate model simulations.

1. Introduction

Clouds are crucial drivers of change in weather and climate systems, and affect the Earth's energy budget and hydrologic cycle via radiative forcing induced by dynamic and thermodynamic processes in the atmosphere (Clement et al., 2009; Boucher et al., 2013; Zhou et al., 2016). The radiative effects of clouds critically depend on cloud vertical structures (CVSs), including cloud top height (CTH), cloud base height (CBH) and cloud layer thickness, which together play significant roles in large-scale atmospheric circulation by altering the gradients of the total diabatic heating/cooling (Webster and Stephens, 1984). For instance, CBH can substantially influence the energy exchanges between cloud layers and the ground surface (Wild, 2012). Moreover, observed changes in the properties of clouds and precipitation are significantly associated with increases in atmospheric levels of both greenhouse

gases and aerosols (Koren et al., 2004; Wang et al., 2015; Li et al., 2016; Guo et al., 2017, 2018).

CVSs have been sufficiently assessed using radiosonde (Narendra Reddy et al., 2018), aircraft (Chen et al., 2016a), and ground- and satellite-based remote sensing techniques (McGill et al., 2002; Yang et al., 2015). Radiosondes can penetrate cloud layers to obtain in situ measurements of temperature, relative humidity, wind, and pressure profiles, which are used to estimate CVSs (Poore et al., 1995; Wang and Rossow, 1995). For example, Chernykh et al. (2001) successfully estimated the CBH, CTH, and cloud amount using soundings taken from 795 radiosonde stations worldwide for the period of 1964–1998. Sun et al. (2007) synthetically analyzed temporal trends in CTH and the frequency of cloud occurrence over the United States since the early 1950s using datasets from radiosondes operated by the National Weather Service and military stations. Zhang et al. (2018b) elucidated
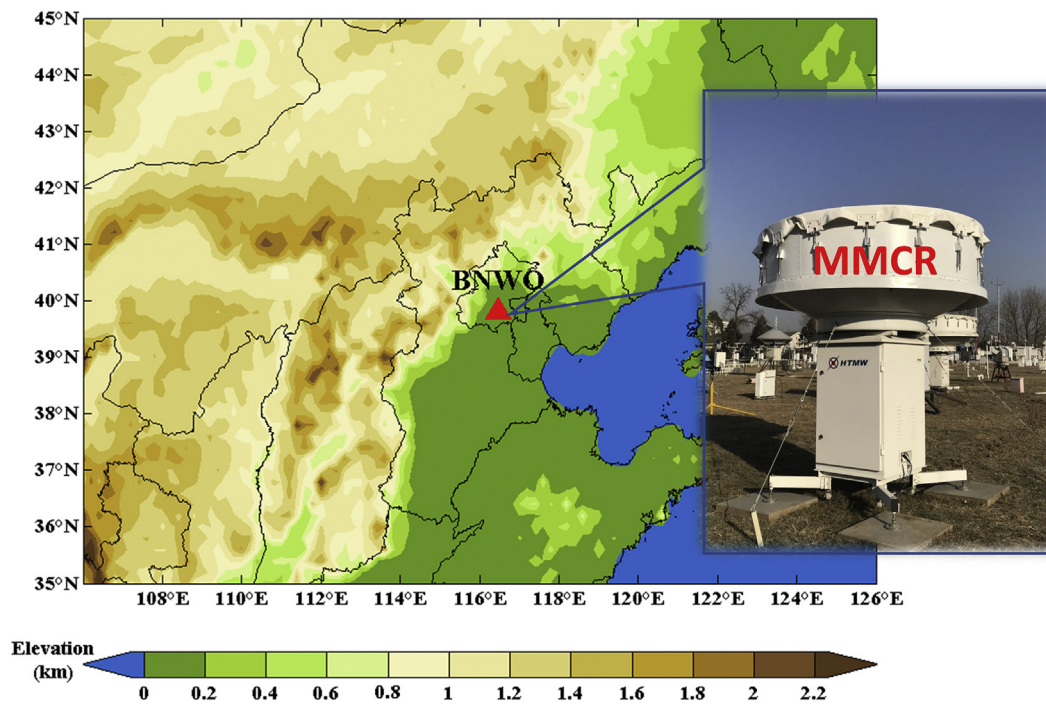
Fig. 1. Ka-band Millimeter-Wave Cloud Radar (MMCR) installed in Beijing Nanjiao weather observatory (BNWO, 39.81°N, 116.47°E, 32 m above sea level).

the seasonal and diurnal variability of CBH over China for the period of 2006–2016 based on fine-resolution sounding observations from the China Radiosonde Network. Nevertheless, radiosondes are only operated twice per day from a limited number of stations (Guo et al., 2016b; Zhang et al., 2016); therefore, cloud observations are temporally and spatially limited.

In situ cloud measurements by aircraft provide reliable measurements of myriad cloud properties but are very costly and provide limited observations because they only provide instantaneous data during a specific time period and over particular region (Aydin and Singh, 2004). Meanwhile passive satellite sensors onboard geostationary satellite, such as the Himawari-8 (HW8), merely make large-scale observations of cloud tops (Chen et al., 2018, 2019). Ideally, three-dimensional structures of clouds are assessed by active satellite sensors onboard polar-orbiting satellites such as CloudSat and CALIPSO at both regional and global scales (Stephens, 2005). The CVSs of clouds over China (Chen et al., 2016b) and East Asia (Yin et al., 2013, 2015) have been investigated based on CloudSat data. However, CloudSat data tend to miss optically thin cirrus clouds and have a relatively low temporal resolution (Guo et al., 2016a).

In contrast, ground-based remote sensing instruments such as lidars (Borg et al., 2011), ceilometers (Martucci et al., 2010), and millimeter wavelength cloud radars (MMCR; Moran et al., 1998) can provide CVSs with a higher precision and continuous temporal coverage. As low-energy lidars, laser ceilometers have been used to measure CBHs at national scales via modernized meteorological observational networks, such as over Spain (Cazorla et al., 2017) and the United States (Dai et al., 2006). Moreover, ground-based cloud radar observations were used to assess the properties of cirrus clouds during the period of 1999–2005 at two Atmospheric Radiation Measurement Program sites (Deng and Mace, 2008). Notably, MMCRs can penetrate clouds and continuously monitor the evolution of CVSs (Hollars et al., 2004) and the microphysical characteristics of clouds, such as the liquid water content, effective radius, and size distribution of cloud droplets (Fox and Illingworth, 1997; Zhao et al., 2017). This is largely due to the higher sensitivity of MMCRs to hydrometeors.

While the gross features of cloud boundaries can be readily obtained by any active lidar or radar, the acquisition of precise CVSs using a single instrument remains challenging (Clothiaux et al., 2000). This is largely due to the significant attenuation caused by precipitation (Kollias et al., 2007). Therefore, the synergic use of surface- and satellite-based active sensors (radar and lidar) is believed to be an ideal tool for such measurements because of their individual complementary and superior capabilities for detecting the properties of clouds (Liu et al., 2017).

Beijing, the capital of China, has been increasingly experiencing severe storms due to the deterioration in air quality caused by global warming (Guo et al., 2011; Mao et al., 2015; Li et al., 2016, 2017), posing a threat to human health and economic growth. Although the CTH or CBH values obtained using MMCRs and other instruments have been compared in several studies (Wang et al., 2018b), no attempts have been made to analyze the characteristics of the distribution of long-term CVSs in Beijing, and the characteristics of cloud structures in Beijing remain poorly understood. This is mainly due to the scarcity of long-term ground-based cloud radar measurements. In 2013, a Ka-band MMCR was installed by the Meteorological Observation Center of the China Meteorological Administration (CMA) at Beijing Nanjiao weather observatory (BNWO; 39.81°N, 116.47°E, 32 m above sea level). This is expected to improve our understanding of convection initiation processes by providing vertical information about the heterogeneous cloud formations, both throughout space and over time (Behrendt et al., 2011).

Therefore, the goal of this study was to investigate the CVSs and their seasonal and diurnal variations based on three years (January 2015 to December 2017) of Ka-band MMCR observations taken from BNWO. The remainder of this paper proceeds as follows: in Section 2, we describe the data and methods. We present our results on the vertical structures and seasonality of clouds in Beijing in Section 3, followed by analyses and discussion of the discrepancy between the MMCR- and ceilometer-derived CBH measurements, as well as the discrepancy between the MMCR- and HW8-derived CTH values. We also investigated the impact of the thickness of the cloud layer on the CBH and CTH. Finally, our key findings are summarized in Section 4.

2. Data and methods

2.1. MMCR cloud observations and miscellaneous data

The Ka-band Doppler MMCR used in this study is located at BNWO (Fig. 1), which is also equipped with ceilometers, a rain gauge, and total sky imager (TSI). This MMCR is designed to point to a height of up to 15 km, with a vertical resolution of 30 m and a temporal resolution of 1 min. The MMCR produces three main basic measurements: radar reflectivity factor, Doppler velocity, and Doppler spectrum width. Here, we analyzed the results of cloud measurements taken between January 1, 2015 and December 31, 2017.

Prior to climatological analyses of cloud structures in Beijing, it was necessary to carry out a comparison and verification study using the Vaisala CL51 ceilometer (CL51) and AHI/HW8. The CL51 is a single-wavelength (near-infrared 910 nm) backscatter lidar, and transmits vertical pulsed waves. It is capable of determining the altitude of clouds automatically and continuously, with a temporal resolution of 1 min and a vertical resolution of 15 m. CBH is obtained from CL51 using a non-standard instrument method (Wang et al., 2018a). The AHI on-board the HW8, as part of the new-generation of Japanese meteorological satellites, has 16 wavelengths, ranging from 0.47 to 13.3 μm, and has been used widely to detect the tops of diverse clouds (Chen et al., 2018; Shang et al., 2018). The CTHs were calculated from the AHI/HW8 measurements using the Fengyun geostationary algorithm testbed-imager (FYGAT-I), which was developed by the Fengyun-4 (FY4) algorithm working group (Min et al., 2017). This imager has a temporal resolution of 10 min and a spatial resolution of 2 km. Considering the various resolutions of the different data sources, the measurement of the CL51 and MMCR were extracted at 10-min intervals to match the AHI/HW8 observations. We also obtained the gridded CTH values of the areas around BNWO from AHI/HW8.

We obtained the visible radiation distribution of the sky using the TSI installed at BNWO, which takes a total-sky photo every 10 min with a resolution of 4288×2848 pixels. This enables us to distinguish clouds in a clear sky based on the fact that radiation from the sky decreases as the number of clouds in the field of view increases. BNWO also hosts a tapered element oscillating microbalance series 1405 (TEOM RP1405; Rupprecht & Patashnick Co., Inc., Albany, NY, USA), with a URG $PM_{2.5}$ cyclone inlet and a PM_{10} cyclone inlet (Ayers et al., 1999). Certified by the United States Environmental Protection Agency, TEOM RP1405 employs an integrated observation method based on an oscillating microbalance and membrane dynamic measurement system to obtain the ambient particulate mass concentration with a temporal resolution of 5 min. The automatic weather station (AWS) at BNWO, which takes measurements of temperature, humidity, wind, pressure, rainfall, visibility, cloud amount/low cloud amount, weather phenomena, etc., is operated by the CMA to supply fundamental observations for weather forecasting and atmospheric research.

2.2. Determination of CTH and CBH from the MMCR

We calculated CBH and CTH based on the boundaries of the clouds detected by the MMCR. First, we used a neural network algorithm to filter out random noise and non-meteorological radar echoes. Second, the cloud boundaries were identified based on the minimum threshold method using radar reflectivity measurements, the minimum of which was set as -40 dBZ. Then, the thickness of each cloud layer and the spaces between adjacent cloud layers were determined. However, single-layer clouds (e.g., cumulus, cumulonimbus, and stratocumulus) containing lots of gaps, tended to be mistaken for multiple-layer clouds. To minimize this effect, we carried out quality control on the cloud boundaries obtained in the previous step by applying the methods proposed by Wang et al. (2018a). Finally, robust cloud boundaries were identified.

Fig. 2a and b present a comparison between two time-height cross-sections of the MMCR-observed radar reflectivity between 0000 and 1900 LST on April 4, 2017, corresponding to the pre- and post- data quality control phases, respectively. According to the 3-h AWS observations, the low cloud cover was 0 at 0800, 1100, 1400, and 1700 LST and the weather was recorded as "haze" during this period. Quantitative data of both ground-based visibility and $PM_{2.5}$ provided further evidence of this episode of atmospheric pollution (Fig. 2c). Because the height of the boundary layer height is generally below 2.5 km in Beijing (Guo et al., 2016b; Zhang et al., 2018a), the continuous radar echo below 2.5 km shown in Fig. 2a may be noise arising from contamination due to aerosol particles. Hence, these data were deleted. We verified the reasonability of the CBH estimates from the MMCR and CL51 by assessing the level of consistency between them (Fig. 2b). Fig. 3 presents another case from July 15, 2017. The TSI images indicated that there were no apparent aerosol layers in the boundary layer at 1640 LST, and no low-level clouds at 1910 LST. This was inconsistent with the low-level radar echo shown in Fig. 3a, possibly due to the presence of ground clutter. Therefore, we removed these signals from Fig. 3b.

Here, cloud layer thickness was defined as the difference between CBH and CTH. We used the aforementioned methods to obtain the CBH, CTH, and cloud layer thickness over three years based on MMCR measurements (January 1, 2015, to December 31, 2017).

2.3. Normalized contoured frequency by altitude diagrams

The contoured frequency by altitude diagram (CFAD) was first proposed by Yuter and Houze Jr. (1995a) in an attempt to show the occurrence frequency (OF) distribution of certain radar reflectivity (Z) values at each altitude level. Because spuriously high OFs can occur at altitudes where there are not enough data points in the CFAD, an improved CFAD, also known as the normalized CFAD (NCFAD), has been developed (e.g., Fu et al., 2003; Guo et al., 2018) to elucidate the fine vertical structures of Z using MMCR readings. The NCFAD is calculated as:

$$\text{NCFAD}(i,j) = \frac{N_z(i,j)}{\sum_{i=1}^{h}\sum_{j=1}^{n} N_z(i,j)} \tag{1}$$

where $N_z(i,j)$ is the frequency distribution function defined as the number of observations in the jth dBZ at the ith level (at intervals of 300 m). Specifically, samples less than -40 dBZ (clear sky) were omitted, in addition to data below 0.3 km (contaminated by ground clutter). As such, the NCFAD was obtained based on the OF of Z at intervals of 1 dBZ across a vertical distance of 300 m.

We also used the NCFADs to investigate the differences between the decibel relative to Z values of precipitating clouds and non-precipitating clouds in different seasons. Unless otherwise stated, precipitating clouds were defined as the occurrence of rain > 0.1 mm/h, according to the rain gauge at BNWO.

2.4. Calculation of cloud frequency and its diurnal variability

Given the temporal resolution of 1 min for the MMCR, a total of 1,578,240 valid MMCR observations were obtained for study period (2015–2017). Cloud OF is defined as the ratio of the number of clouds detected by all valid MMCR observations. We defined two cloud OF (COF) metrics for subsequent analysis. One is the cloud cover occurrence frequency (CCOF), which is defined as the ratio of the number of times that a cloud is detected by valid MMCR observations to the total number of valid observations. The second metric is based on the vertical profiles of CBH and CTH and is counted using the same method as the CCOF, except that it is limited to altitude intervals of 500 m, ranging from the ground to the top of the atmosphere. This enabled us to identify the altitudes at which the cloud top/base was most probably located according to the MMCR. These most probable heights (MPHs)
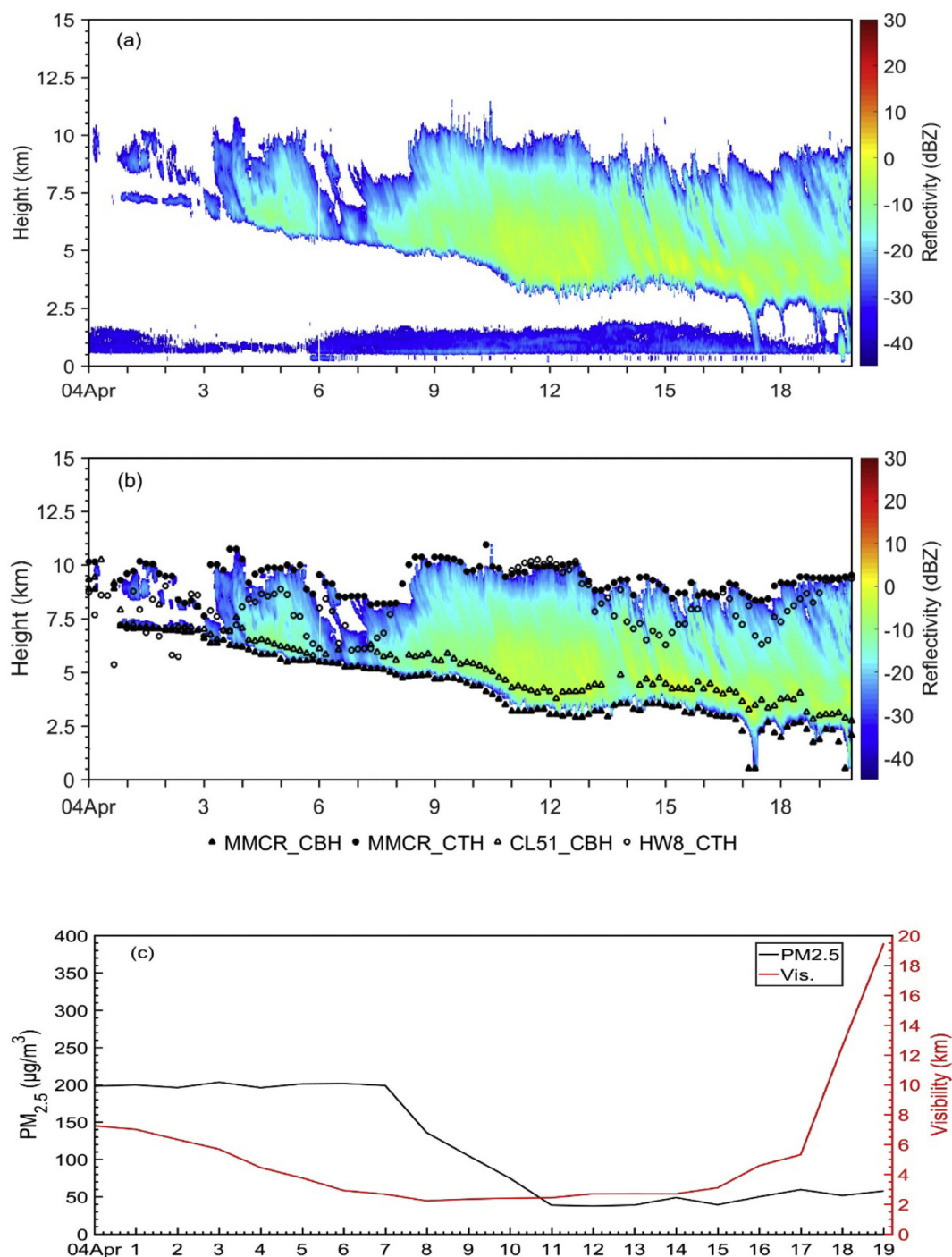
Fig. 2. The time-height cross section of MMCR-observed radar reflectivity before (a) and after (b) quality control, superimposed by MMCR- (solid triangles) and CL51-derived CBHs (hollow triangles) and MMCR- (solid circles) and HW8-derived CTH (hollow circles), and (c) the times series of PM2.5 and visibility data at BNWO from 0000 to 1900 Local Standard Time (LST) on 4 April 2017.

were evaluated based on the vertical frequency of CBH and CTH throughout the entire atmospheric column (Huang et al., 2015).

Finally, we investigated the effect of cloud layer thickness on the CVS by analyzing the joint dependence of cloud frequency on CTH and cloud layer thickness by plotting a two-dimensional frequency diagram.

3. Results and discussion

3.1. CVS and seasonal variation

Fig. 4 shows the NCFADs of precipitating clouds in different seasons

during the period of 2015 to 2017. Furthermore, we superimposed the profiles of the mean values and 90% of the reflectivity range of pre-cipitating and non-precipitating clouds. In general, CTH could reach an altitude exceeding 14 km, and the maximum radar reflectivity exceeded 38 dBZ in the case of precipitating clouds, which were mainly located at altitudes of 1–10 km, with reflectivities ranging from -20 dBZ to 10 dBZ. The maximum frequency of reflectivities exceeding -15 dBZ was located at an approximate height of 7 km, while the maximum re-flectivity was located at lower levels. These results were similar to those reported by Zhang et al. (2006), who used CFADs and mean vertical profiles to analyze the structures of different types of meso-β-scale
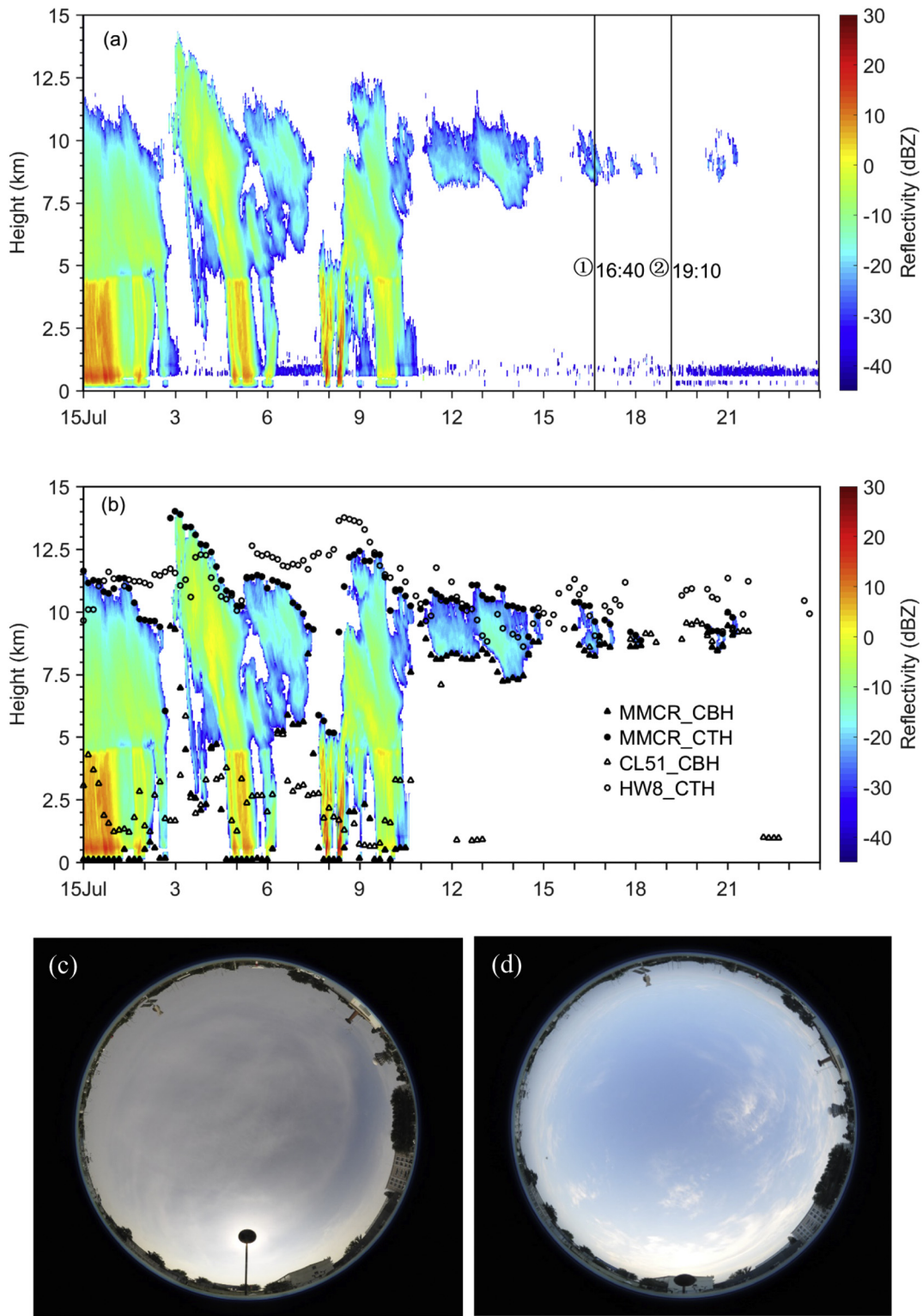
Fig. 3. (a) and (b) are the same as Fig. 2 but for the period from 0000 to 2359 LST on 15 Jul 2017. Photos taken by Total Sky Imager (TSI) at 1640 LST (c) and 1910 LST (d) on 15 Jul 2017, respectively.

convective systems around the Meiyu front. In contrast, non-precipitating clouds were mainly located at heights of 2–12 km (Fig. 5), and the radar reflectivity varied between −28 and 0 dBZ. The maximum frequency occurred at a height of 7–9 km, with a radar reflectance ranging from −26 to 24 dBZ. Compared with precipitating clouds, non-precipitating clouds tended to occur at higher altitudes, had weaker reflectivities, and were usually well above ground.

Both precipitating clouds and non-precipitating clouds exhibited marked seasonal variation. CTH could reach 11 km in spring and the maximum reflectivity was 32 dBZ in the case precipitating clouds, which mainly occurred at heights of 1–9 km, with the reflectivity ranging from −30 to 15 dBZ. The radar reflectivity profile decreased as the height increased up to 4 km, increased slightly between 4 and 5 km, and decreased sharply thereafter (Fig. 4a). At altitudes of 2–4 km, the
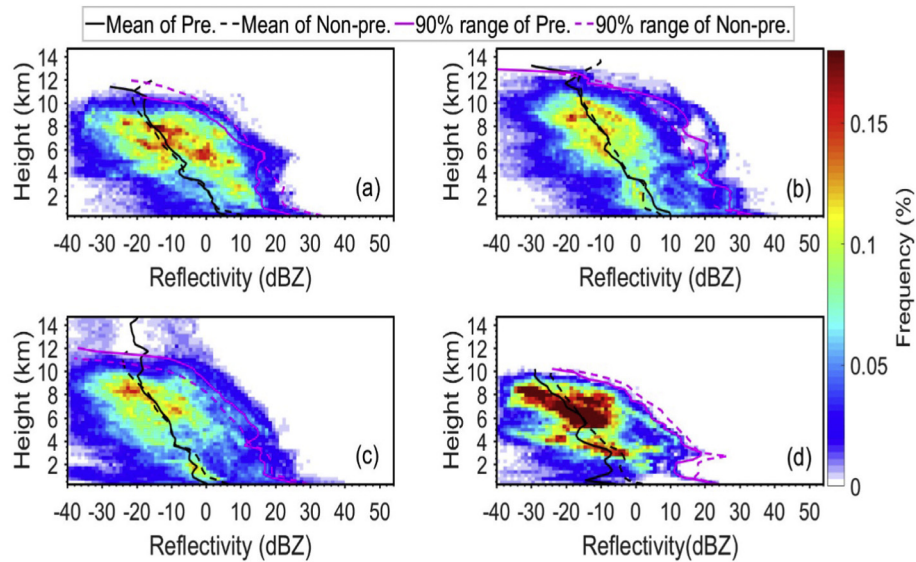
Fig. 4. Normalized contoured frequency by altitude diagram (NCFAD) for precipitating clouds in spring (a), summer (b), autumn (c), winter (d), superimposed with profiles of mean and highest 90% reflectivity for precipitating clouds and non-precipitating clouds, respectively. The occurrence frequency (in %) is calculated for each grid with 1 dBZ in reflectivity and 0.3-km in height. White areas represent the grids with occurrence frequency below 0.003%.
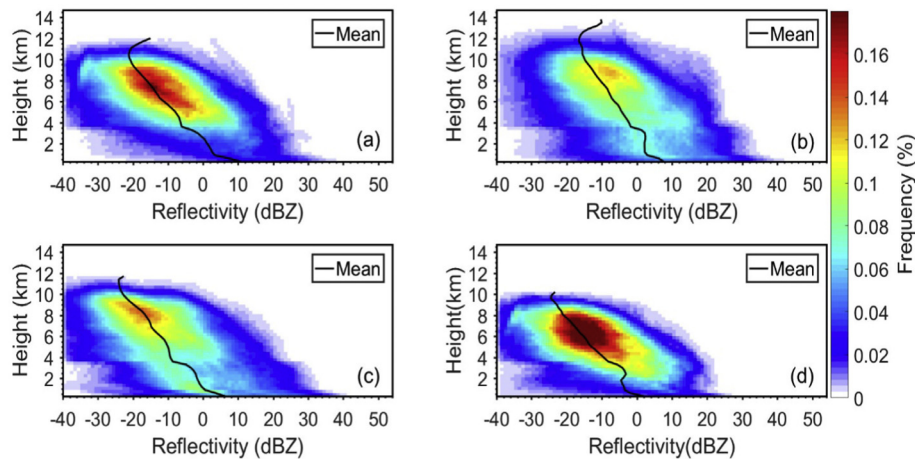

Fig. 5. As in Fig. 4 but for non-precipitating clouds in spring (a), summer (b), autumn (c), winter (d), superimposed with profiles of mean reflectivity for non-precipitating clouds.
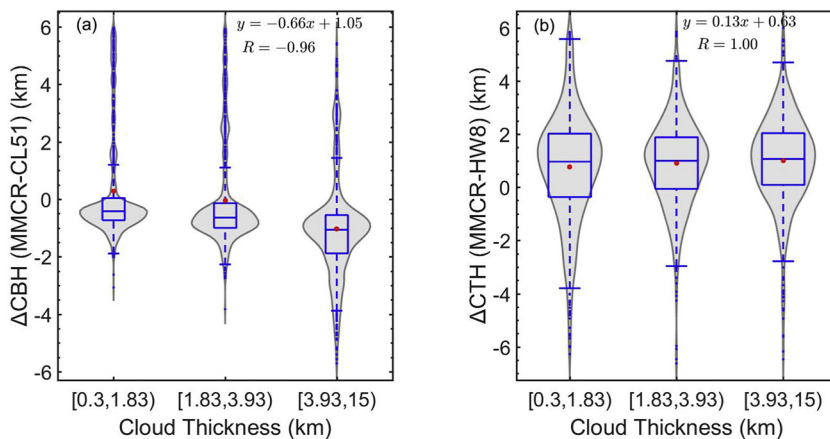

Fig. 6. Kernel density estimation between cloud layer thickness and ΔCBH (MMCR minus CL51) (a) and ΔCTH (MMCR minus HW8) (b), which has binned by equal number of samples in the case of non-precipitating clouds. The boxes in blue represent the maximum, minimum, median and 50% range of the data in each interval. Red dots represent the mean value of each interval. The gray shading areas represent the probability of samples, and R denotes the correlation coefficient between mean values for each interval of ΔCBH (ΔCTH) and cloud layer thickness. (For interpretation of the references to colour in this figure legend, the reader is referred to the web version of this article.)

reflectivity was weak and showed a steep gradient (~5 dBZ/km), indicative of rapid cloud droplet growth. The reflectivity peaks then remained constant at an altitude of 1–2 km, indicating that cloud droplet growth slowed and cloud droplet began to accumulate in this layer. At altitudes below 1 km, the intensity of reflectivity started to strengthen, suggesting that the size and concentration of raindrop particles

increased due to a collision/coalescence process. This distribution pattern is not only related to the microscopic growth of particles, but also their final velocity and the distribution of updraft (Yuter and Houze Jr., 1995b).

Compared to spring, clouds tended to develop at much higher altitudes and more intensely in summer, with CTHs reaching 13 km and
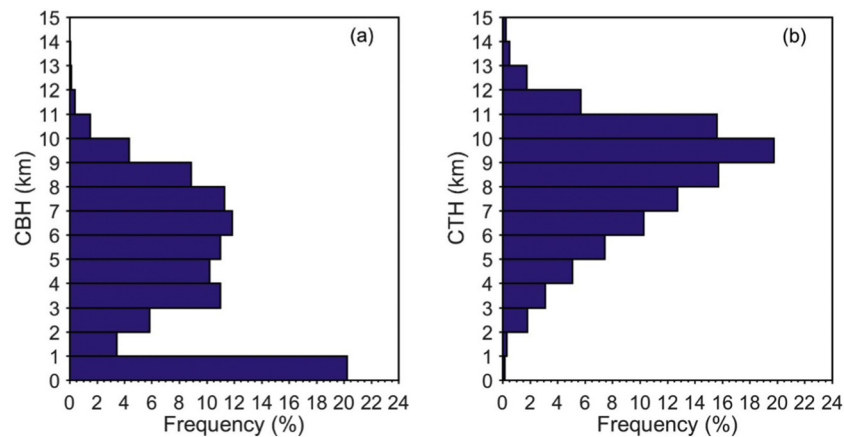
Fig. 7. Histogram of CBHs (a) and CTHs (b) as observed by MMCR installed at BNWO for the period 2015 to 2017.
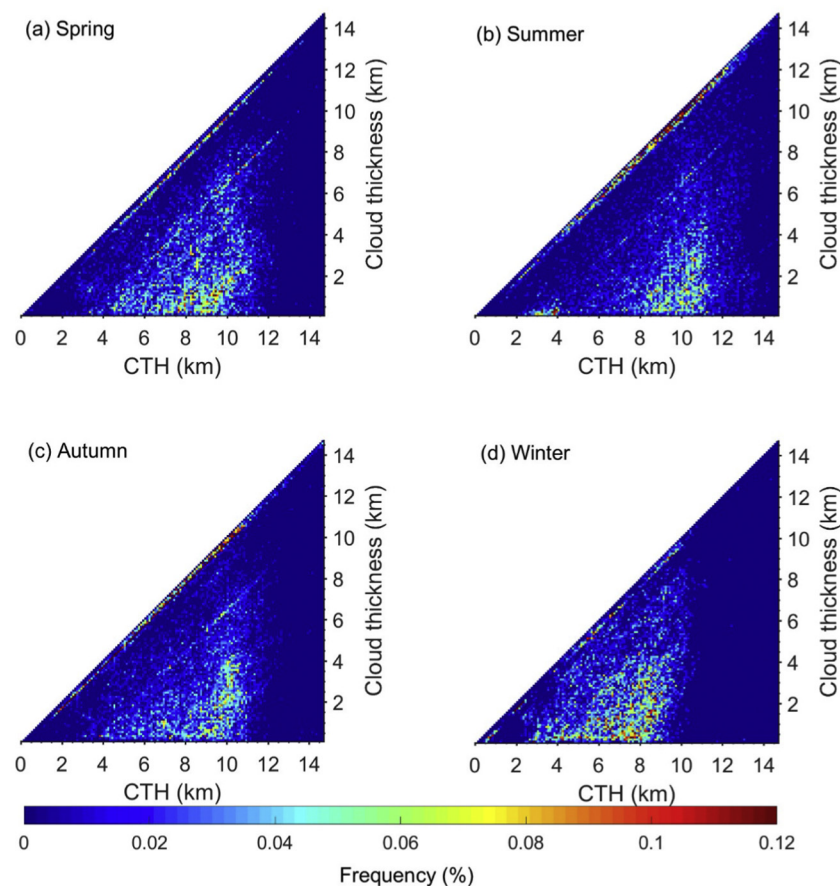

Fig. 8. Two-dimensional frequency distribution of CTH and cloud layer thickness in Beijing in spring (a), summer (b), autumn (c), winter (d) for the period 2015 to 2017.

reflectivities exceeding 40 dBZ. Furthermore, the reflectivity was larger at heights below 4 km and the height of the maximum of frequency increased slightly (Fig. 4b). This may be due to the prevalence of convective clouds in summer (Li et al., 2016). In autumn, the NCFAD pattern of precipitating clouds resembled that of summer, albeit with higher CTHs (> 14 km). The CTH of precipitating clouds was lowest in winter (< 10 km), and the maximum radar reflectivity was also reduced to 24 dBZ (Fig. 4d). Another interesting feature was the presence of two peaks in the vertical profile in winter: one located at 1.5–3.5 km, with reflectivities between −10 and 8 dBZ, and the other located at 6–8 km with reflectivities between −30 and −5 dBZ. These peaks were probably related to the deposition and freezing processes of ice particles

in solid precipitating clouds. The vertical profile of the reflectivity was similar to those reported previously, in which radar reflectivity decreased gradually with increasing height in the case of rain thunderstorms, and the maximum of the profile and its height both increased with the severity of precipitation (e.g., Xu et al., 2009). The vertical structure of non-precipitating clouds was similar to that of precipitating clouds, decreasing gradually with height (Fig. 5).

Overall, the vertical structures and seasonality of clouds obtained from the three years of MMCR observations bore some resemblance to those reported in several pioneering studies (e.g., Luo et al., 2009; Yin et al., 2013), where the CVSs of clouds in Beijing were analyzed based on either MMCR or CloudSat measurements. The results of these studies
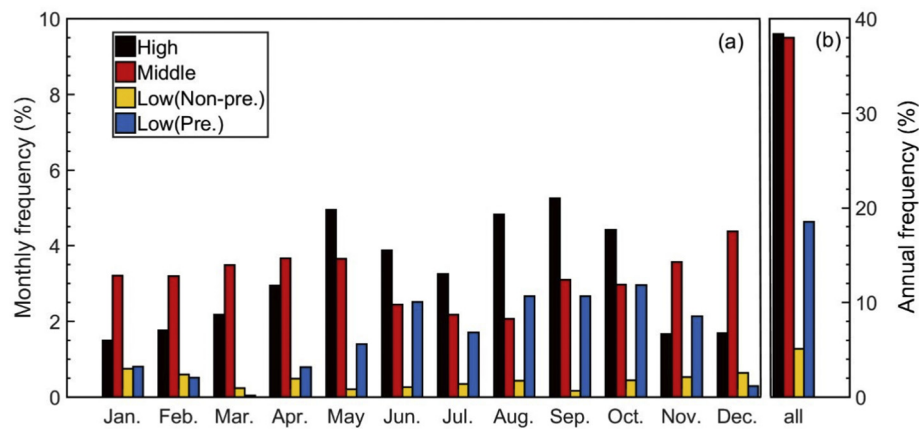
Fig. 9. Occurrence frequency of diverse cloud regimes in each month (a) and during the entire years around (b) as observed by MMCR in Beijing during the period 2015 to 2017.
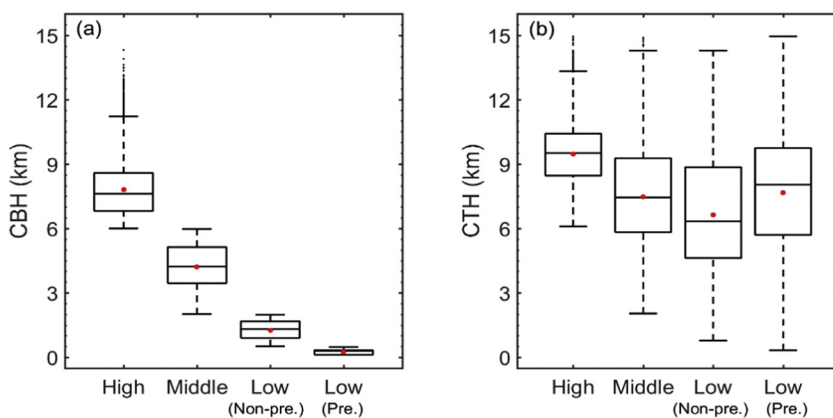

Fig. 10. Box plots of CBH (a) and CTH (b) for various cloud types. Boxes denote the 25th and 75th percentile positions whereas the lines and red dots inside the box show the median and mean values, respectively. (For interpretation of the references to colour in this figure legend, the reader is referred to the web version of this article.)

showed that the maximum frequency of the reflectivity occurred in winter and spring and the echo top height peaked in summer and was lowest in winter.

3.2. Comparison of MMCR- and CL51/HW8-derived CBH and CTH

We assessed the robustness of the CBH and CTH measurements from the MMCR at BNWO by comparing them with the CBH and CTH values obtained using the CL51 and HW8, respectively. We counted 4921 cloud occurrences over a yearlong observational period, simultaneously based on the measurements from the MMCR, CL51, and HW8. The average CBH according to the MMCR was slightly higher (0.08 km) than that of the CL51. The CTH from the MMCR was much higher (average: 0.82 km) than the value from the HW8. Because we used millimeter-wavelength signals to detect small cloud particles, strong MMCR signal attenuation occurred during precipitation, which accounted for the lower CTH values observed using the MMCR.

To better understand the distribution of ΔCBH (MMCR minus CL51) and ΔCTH (MMCR minus HW8) values in light of the cloud layer thickness in non-precipitating clouds, we estimated the kernel probability density of these differences and cloud layer thickness (Fig. 6). In general, the CBH (CTH) values from the MMCR and CL51 (HW8) were in good agreement, with correlation coefficients of up to 0.96 (1.00). Overall, the MMCR tended to overestimate CTH but underestimate CBH. In particular, the ΔCTHs were larger in the case of thin clouds than thick clouds. This can be partly explained by the methods used to calculate CTH, which rely heavily on the infrared channels of the geostationary satellite. When clouds are thin, the radiative energy received by HW8 inevitably contains information from the surface below the cloud, increasing the brightness temperature. This tended to make

the cloud top detected by HW8 much lower than that detected by the MMCR. In contrast, the magnitude of the CTH obtained from HW8 when the clouds were thick agreed well with that obtained from the MMCR.

3.3. Statistical characteristics of MMCR-derived CBH and CTH

Fig. 7 shows the height-resolved frequency distributions of both CBH and CTH. There were two MPHs for the CBHs of the three-year MMCR observations, corresponding to heights of 0–1 km and 5–6 km (Fig. 7a). One striking feature was that 20.2% of the CBHs were lower than 1 km, probably due to the fact that most of the cloud bases derived from the MMCR were close to the ground, especially during precipitation. Furthermore, it is extremely difficult to discriminate between cloud and precipitation droplets, which causes the MMCR to significantly underestimate CBH (Oh et al., 2016). Meanwhile, 89% of the CTHs were higher than 5 km (Fig. 7b), with the maximum frequency (19.7%) occurring at altitudes of 9–10 km. This was similar to previous satellite findings (e.g., Chen et al., 2018). In general, the vertical frequency distribution of CBHs and CTHs indicated that middle- and high-level clouds dominated in Beijing during the observation period. Compared with previous observations from CloudSat (e.g., Wang et al., 2011), the average CBH, CTH, and MPH obtained from the MMCR measurements over the more recent three-year study period were slightly higher. However, the cited studies only investigated the CBHs and CTHs of particular cloud types over China from 2006 to 2009. More importantly, the expansion of urbanization in Beijing inevitably increases the urban heat island effect, which leads to elevated lift condensation levels and in turn increases the CBH (Mote et al., 2007; Williams et al., 2015). Furthermore, the cloud systems traveling
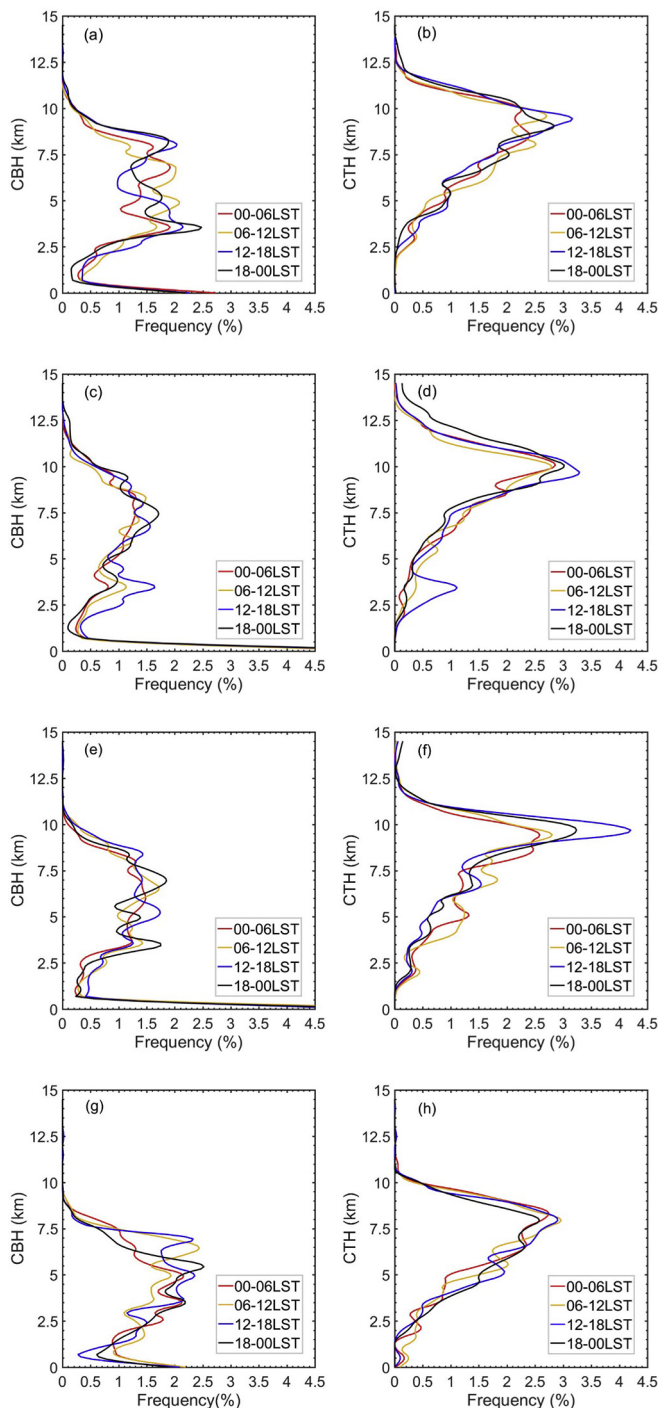
Fig. 11. The vertical distribution of diurnal occurrence frequency of CBHs (a, c, e, g) and CTHs (b, d, f, h) at 6 h intervals in spring, summer, autumn and winter respectively. Samples are vertically divided with a resolution of 500 m. The percentage for a given altitude is defined as the ratio of cloudy samples on that altitude to all cloudy samples.

southward over the urban areas of Beijing tend to be split due to the enhanced urban heat island effect (Dou et al., 2015). This could lead to changes in the cloud frequency observed at the BNWO.

Fig. 8 shows the two-dimensional frequency distribution of CTH and cloud layer thickness during the four seasons. In summer, most data pairs were along the 1:1 line, that is to say, the thickness of thick clouds increased almost linearly with CTH. Therefore, we inferred that clouds readily form as deep convection clouds in summer, with CTHs of 8–12 km. This is due to the strong solar radiation and East Asian
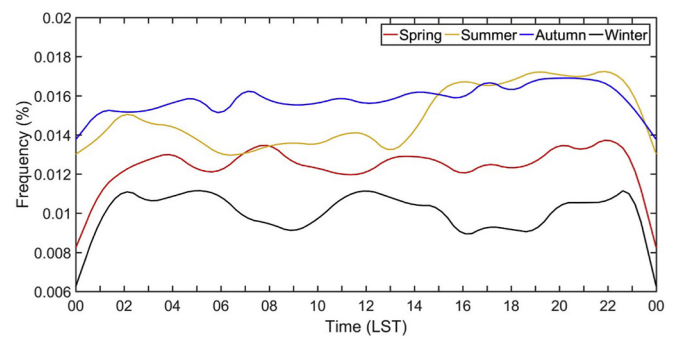

Fig. 12. Diurnal cycle of mean cloud cover occurrence frequency in different seasons.

Summer Monsoon during summer (Li et al., 2016). In contrast, the clouds with CTHs of < 8 km and cloud layer thicknesses of < 4 km tended to occur more often in winter. It was challenging to discriminate between the joint frequency distribution patterns in spring and autumn.

According to the cloud classification method proposed by Wang et al. (2018a), we used the CBH and CTH results to categorize the clouds as high (CBH ≥ 6 km), middle (2 km ≤ CBH < 6 km), and low (CBH < 2 km) clouds. Furthermore, low clouds were divided into non-precipitating and precipitating low-level clouds. Over the entire observation period, high clouds occurred most frequently (38.4%), followed by middle clouds (38.0%), low-level precipitating clouds (18.5%), and low-level non-precipitating clouds (5.1%). This supports the hypothesis that middle- and high-level clouds are dominant in Beijing (Fig. 9). Regarding the frequencies of various cloud types on a monthly timescale, the aforementioned frequency patterns were largely limited to clouds in May, September, and October, whereas the OF of middle-altitude clouds was highest between November and April. High- and low-level precipitating clouds often occurred in Beijing during the rainy season (May to October), whereas middle-altitude clouds mainly occurred in winter and spring.

Fig. 10 shows box plots of the distributions of the average CBH and CTH for various cloud types that occur in Beijing, according to the MMCR measurements. The mean CBHs of high, middle, low non-precipitating and low precipitating clouds were 7.80, 4.20, 1.27 and 0.26 km, respectively. Meanwhile, the CTHs of high clouds were highest (9.45 km), whereas those of low non-precipitating clouds were lowest (6.64 km). Unsurprisingly, the CTHs of low precipitating clouds were higher than those of low non-precipitating clouds, indicating that low precipitating clouds were often convective, resulting in more elevated cloud tops.

3.4. Temporal evolution of CBH and CTH

The height-resolved radar reflectivity MMCR observations enabled the determination of the temporal evolution of CBH and CTH in the vertical direction. Fig. 11 shows the distribution of the diurnal OFs of the CBHs and CTHs across the four seasons. To ensure that each layer had a sufficient number of samples, we resampled the data to a vertical resolution of 500 m. We calculated the CBH (CTH) frequency by taking the ratio of the number of cloud bottoms (tops) for each 500-m interval every 6 h to the total number of clouds. Regarding the vertical distribution of CTHs (Fig. 11b, d, f, and h), the COF roughly increased with height until 9–10 km, above which the COF dropped dramatically with increasing altitude. From 0000 LST, both the CTH and the probability of cloud-top occurrence increased slightly until the peak time (1200–1800 LST), and then dropped at night time. This suggests that the formation of most clouds with CTHs up to 6 km is associated with solar insolation and strong heat flux over land. Interestingly, the cloud-top OFs were similar for each season. In addition to the peak at 9–10 km, there were additional peaks in cloud-top OF at 2–4 km in summer, 4–6 km in
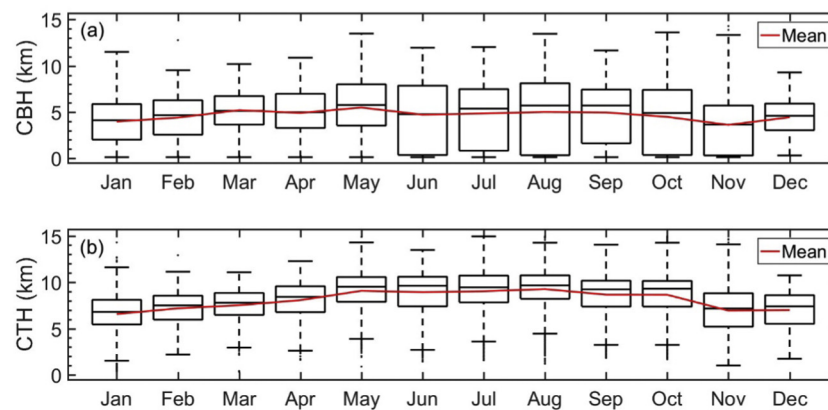
Fig. 13. Annual variation of CBH (a) and CTH (b). Boxes denote the 25th and 75th percentile positions whereas the lines and red dots inside the box show the median and mean values, respectively. (For interpretation of the references to colour in this figure legend, the reader is referred to the web version of this article.)

autumn, and 5–6 km in winter. Clouds with a CTH of 2–4 km tended to occur between 1200 and 1800 LST in summer, indicating that low-level clouds often formed in the late afternoon in summer. Meanwhile, clouds with a CTH of 4–6 km were likely to occur between 0000 and 1200 LST in autumn.

The vertical distributions of the diurnal frequencies of CBHs are shown in Figs. 11a, c, e, and g. These distributions revealed a bimodal pattern, with one mode located at 0.5 km and the other located at altitudes of 3.5–6.5 km. As mentioned above, the CBHs obtained from the MMCR were closer to the ground when it was raining, which at least partly explained the high frequency of CBHs near the ground. Above a height of 1 km, CBHs occurred most frequently at approximately 7 km between 0000 and 1200 LST, then dropped in height to 3.5 km between 1200 and 0000 LST. Hence, the solar radiation incident on the surface increased in the afternoon, which tended to result in a convectively unstable atmosphere, thereby thickening the cloud layer. These results were generally in good agreement with previous findings from radiosondes in China (Zhang et al., 2018b).

Fig. 12 shows the diurnal variation in COF among seasons regardless of the difference between the CTH and CBH. Clouds tended to form most frequently in the afternoon until the evening, in summer and autumn. This agreed well with results obtained from HW8 (Chen et al., 2018). In comparison, there were no apparent diurnal cycles in spring and winter. In terms of seasonality, the maximum frequency over the course of a day peaked in autumn, followed by summer, spring, and finally winter. These findings were in agreement with those reported by Jin et al. (2009).

In terms of annual variation, CBH generally peaked in spring and summer, and reached minima in fall and winter. This differed slightly from the variation in CTH, with peaks in summer and fall and minima in spring and winter (Fig. 13). The strong contrasts between the CBHs and CTHs in different seasons could be due to differences in solar radiation, which exhibits pronounced seasonality, being highest in summer, and thus favoring the development of convective precipitating clouds. Furthermore, the low CBH values in winter are likely associated with temperature minima, facilitating water vapor condensation or collision/coalescence to form cloud droplets under upward-motion conditions, leading to a low CBH. These results are consistent with those reported by Zhang et al. (2018b), who used radiosonde data to analyze the climatology of CBH in China.

4. Conclusions

We analyzed the results of continuous Ka-band MMCR measurements at BNWO over a three-year period (2015–2017), and systematically investigated cloud climatology of the CBH, CTH, and CVS. To our knowledge, this is the first analysis of the climatology of cloud

properties to elucidate their vertical structures and temporal distributions in Beijing using an MMCR.

Precipitating clouds mainly occurred at altitudes of 1–10 km, with reflectivity varying from −20 to 10 dBZ, whereas non-precipitating clouds generally occurred at heights of 2–12 km, and had weaker reflectivities ranging from −28 to 0 dBZ. In terms of seasonal variation, CTH and radar reflectivity were higher in summer and autumn than spring and winter, which experience less convective precipitation. From the perspective of the vertical reflectivity profiles, the reflectivities of both precipitating and non-precipitating clouds decreased from the surface to high altitudes. Seasonally, the vertical structures of non-precipitating clouds did not vary significantly, whereas the center of the maximum reflectivity frequency did vary.

Compared to measurements from HW8 and CL51, the average MMCR-derived CBH was 0.08 km higher than that of CL51, whereas the average MMCR-derived CTH was 0.82 km higher than that of HW8. Intriguingly, the discrepancies between the CTH measurements from the MMCR and HW8 decreased as the cloud layer thickness increases, due to the manner in which the satellite infrared channel measures CTH.

In the vertical direction, there were two CBH peaks, located at 0–1 km and 5–6 km, respectively, whereas CTH occurred most frequently at altitudes of 9–10 km. In the case of the diurnal cycle of the vertical cloud profiles, both CTH and the probability of cloud-top occurrence increased from 0000 LST until the peak time, between 1200 and 1800 LST, and then dropped at night. Meanwhile, the peak CBH probability was higher between 0000 and 1200 LST than between 1200 and 0000 LST. The mean cloud cover frequency generally followed a downward trend from autumn to winter, which varied markedly from the trend observed in summer, in which the peak cloud occurrence occurred between 1500 and 2000 LST.

Some aspects of this study require further refinement in the future. For example, we did not consider the influence of multiple-layer clouds. MMCR measurements can also be used to measure the microphysical properties of clouds (e.g., particle size, concentration, and water content) and dynamic processes (e.g., vertical velocity). These data can then be analyzed by researchers studying severe weather phenomena, such as the downbursts that are typically produced by high cumulonimbus clouds (Burlando et al., 2017). Therefore, these issues merit further analysis in separate studies. More importantly, it remains challenging to predict the composite radar reflectivity (Lompar et al., 2017, 2018), even though the 3DVar assimilation method can be used to assimilate the cloud radar observations (e.g., Borderies et al., 2018). Therefore, much more efforts should be devoted to explicit model work by using more advanced assimilating methods in the future.

Acknowledgements

References

Aydin, K., Singh, J., 2004. Cloud ice crystal classification using a 95-GHz polarimetric radar. J. Atmos. Ocean. Technol. 21, 1679–1688. https://doi.org/10.1175/jtech1671.1.

Ayers, G.P., Keywood, M.D., Gras, J.L., 1999. TEOM vs. manual gravimetric methods for determination of $PM_{2.5}$ aerosol mass concentrations. Atmos. Environ. 33, 3717–3721.

Behrendt, A., Pal, S., Aoshima, F., et al., 2011. Observation of convection initiation processes with a suite of state-of-the-art research instruments during COPS IOP 8b. Q. J. R. Meteorol. Soc. 137, 81–100. https://doi.org/10.1002/qj.758.

Borderies, M., Caumont, O., Delanoë, J., Ducrocq, V., Fourrié, N., Marquet, P., 2018. Impact of airborne cloud radar reflectivity data assimilation on kilometre-scale NWP analyses and forecasts of heavy precipitation events. Nat. Hazards Earth Syst. Sci. Discuss. https://doi.org/10.5194/nhess-2018-314.

Borg, L.A., Holz, R.E., Turner, D.D., 2011. Investigating cloud radar sensitivity to optically thin cirrus using collocated Raman lidar observations. Geophys. Res. Lett. 38, L05807. https://doi.org/10.1029/2010GL046365.

Boucher, O., Randall, D., Artaxo, P., et al., 2013. Clouds and aerosols. In: Stocker, T.F., Qin, D., Plattner, G.-K., Tignor, M., Allen, S.K., Boschung, J., Nauels, A., Xia, Y., Bex, V., Midgley, P.M. (Eds.), Climate Change 2013: The Physical Science Basis. Contribution of Working Group I to the Fifth Assessment Report of the Intergovernmental Panel on climate Change. Cambridge University Press, Cambridge, United Kingdom and New York, NY, USA.

Burlando, M., Romanić, D., Solari, G., Hangan, H., Zhang, S., 2017. Field Data Analysis and Weather scenario of a Downburst Event in Livorno, Italy, on 1 October 2012. Mon. Weather Rev. 145, 3507–3527. https://doi.org/10.1175/MWR-D-17-0018.1.

Cazorla, A., Casquero-Vera, J.A., Román, R., Guerrero-Rascado, J.L., Toledano, C., Cachorro, V.E., Orza, J.A.G., Cancillo, M.L., Serrano, A., Titos, G., Pandolfi, M., Alastuey, A., Hanrieder, N., Alados-Arboledas, L., 2017. Near-real-time processing of a ceilometer network assisted with sun-photometer data: monitoring a dust outbreak over the Iberian Peninsula. Atmos. Chem. Phys. 17, 11861–11876. https://doi.org/10.5194/acp-17-11861-2017.

Chen, S., Kerns, B., Guy, N., 2016a. Aircraft observations of dry air, the ITCZ, convective cloud systems, and cold pools in MJO during DYNAMO. Bull. Am. Meteorol. Soc. 97 (3), 405–423. https://doi.org/10.1175/BAMS-D-13-00196.1.

Chen, T.M., Guo, J.P., Li, Z.Q., Zhao, C.F., Liu, H., Cribb, M., Wang, F., He, J., 2016b. A CloudSat perspective on the cloud climatology and its association with aerosol perturbations in the vertical over Eastern China. J. Atmos. Sci. 73, 3599–3616. https://doi.org/10.1175/JAS-D-15-0309.1.

Chen, D., Guo, J., Wang, H., Li, J., Min, M., Zhao, W., Yao, D., 2018. The cloud top distribution and diurnal variation of clouds over East Asia: preliminary results from Advanced Himawari Imager. J. Geophys. Res. Atmos. 123 (7), 3724–3739. https://doi.org/10.1002/2017JD028044.

Chen, D., Guo, J., Yao, D., Lin, Y., Zhao, C., Xu, H., Liu, L., Huang, X., Zhai, P., 2019. Mesoscale convective systems in East Asia from Advanced Himawari Imager: Algorithms and preliminary results. J. Geophys. Res. Atmos. 124. https://doi.org/10.1029/2018JD029707.

Chernykh, I.V., Alduchov, O.A., Eskridge, R.E., 2001. Trends in low and high cloud boundaries and errors in height determination of cloud boundaries. Bull. Am. Meteorol. Soc. 82, 1941–1947. https://doi.org/10.1175/1520-0477(2001)082<1941:TILAHC>2.3.CO;2.

Clement, A.C., Burgman, R., Norris, J.R., 2009. Observational and model evidence for positive low-level cloud feedback. Science 325, 460–464. https://doi.org/10.1126/science.1171255.

Clothiaux, E.E., Ackerman, T.P., Mace, G.G., Moran, K.P., Marchand, R.T., Miller, M.A., Martner, B.E., 2000. Objective determination of cloud heights and radar reflectivities using a combination of active remote sensors at the ARM CART sites. J. Appl. Meteorol. 39, 645–665. https://doi.org/10.1175/1520-0450(2000)039<0645:ODOCHA>2.0.CO;2.

Dai, A.G., Karl, T.R., Sun, B.M., Trenberth, K.E., 2006. Recent trends in cloudiness over the United States: a tale of monitoring inadequacies. Bull. Am. Meteorol. Soc. 87, 597–606. https://doi.org/10.1175/BAMS-87-5-597.

Deng, M., Mace, Gerald G., 2008. Cirrus microphysical properties and air motion statistics using Cloud Radar doppler moments. Part II: Climatology. J. Appl. Meteorol. Climatol. 47 (12), 3221–3235. https://doi.org/10.1175/2008JAMC1949.1.

Dou, J., Wang, Y.C., Bornstein, R., Miao, S.G., 2015. Observed Spatial Characteristics of Beijing Urban climate Impacts on Summer Thunderstorms. J. Appl. Meteorol. Climatol. 54, 94–105. https://doi.org/10.1175/JAMC-D-13-0355.1.

Fox, N.I., Illingworth, A.J., 1997. The retrieval of stratocumulus cloud properties by ground-based cloud radar. J. Appl. Meteorol. 36 (5), 485–492. https://doi.org/10.1175/1520-0450(1997)0362.0.CO;2.

Fu, Y., Lin, Y., Liu, G., Wang, Q., 2003. Seasonal characteristics of precipitation in 1998 over East Asia as derived from TRMM PR. Adv. Atmos. Sci. 20, 511–529. https://doi.org/10.1007/BF02915495.

Guo, J.P., Zhang, X.Y., Wu, Y.R., Che, H.Z., Laba, Li, X., 2011. Spatio-temporal variation trends of satellite-based aerosol optical depth in China during 1980–2008. Atmos. Environ. 45 (37), 6802–6811. https://doi.org/10.1016/j.atmosenv.2011.03.068.

Guo, J., Liu, H., Wang, F., Huang, J., Xia, F., Lou, M., Wu, Y., Jiang, J., Xie, T., Zhaxi, Y., Yung, Y., 2016a. Three-dimensional structure of aerosol in China: a perspective from multi-satellite observations. Atmos. Res. 178–179, 580–589. https://doi.org/10.1016/j.atmosres.2016.05.010.

Guo, J., Miao, Y., Zhang, Y., Liu, H., Li, Z., Zhang, W., He, J., Lou, M., Yan, Y., Bian, L., Zhai, P., 2016b. The climatology of planetary boundary layer height in China derived from radiosonde and reanalysis data. Atmos. Chem. Phys. 16, 13309–13319. https://doi.org/10.5194/acp-16-13309-2016.

Guo, J., Su, T., Li, Z., Miao, Y., Li, J., Liu, H., Xu, H., Cribb, M., Zhai, P., 2017. Declining frequency of summertime local-scale precipitation over eastern China from 1970–2010 and its potential link to aerosols. Geophys. Res. Lett. 44, 5700–5708. https://doi.org/10.1002/2017GL073533.

Guo, J., Liu, H., Li, Z., Rosenfeld, D., Jiang, M., Xu, W., Jiang, J.H., He, J., Chen, D., Min, M., Zhai, P., 2018. Aerosol-induced changes in the vertical structure of precipitation: a perspective of TRMM precipitation radar. Atmos. Chem. Phys. 18, 13329–13343. https://doi.org/10.5194/acp-18-13329-2018.

Hollars, S., Fu, Q., Comstock, J., Ackerman, T., 2004. Comparison of cloud-top height retrievals from ground-based 35 GHz MMCR and GMS-5 satellite observations at ARM TWP Manus site. Atmos. Res. 72, 169–186. https://doi.org/10.1016/j.atmosres.2004.03.015.

Huang, J., Guo, J., Wang, F., Liu, Z., Jeong, M.J., Yu, H., Zhang, Z., 2015. CALIPSO inferred most probable heights of global dust and smoke layers. J. Geophys. Res. Atmos. 120, 5085–5100. https://doi.org/10.1002/2014JD022898.

Jin, X., Wu, T.W., Li, L., Shi, C.X., 2009. Cloudiness characteristics over Southeast Asia from satellite FY-2C and their comparison to three other cloud data sets. J. Geophys. Res. Atmos. 114, D17207. https://doi.org/10.1029/2008JD011422.

Kollias, P., Clothiaux, E.E., Miller, M.A., Albrecht, B.A., Stephens, G.L., Ackerman, T.P., 2007. Millimeter-wavelength radar: New frontier in atmospheric cloud and precipitation research. Bull. Am. Meteorol. Soc. 1608–1624. https://doi.org/10.1175/BAMS-88-10-1608.

Koren, I., Kaufman, Y.J., Remer, L.A., Martins, J.V., 2004. Measurement of the effect of Amazon smoke on inhibition of cloud formation. Science 303 (5662), 1342–1345. https://doi.org/10.1126/science.1089424.

Li, Z., Lau, W.K.-M., Ramanathan, V., Wu, G., Ding, Y., Manoj, M.G., Liu, J., Qian, Y., Li, J., Zhou, T., Fan, J., Rosenfeld, D., Ming, Y., Wang, Y., Huang, J., Wang, B., Xu, X., Lee, S.S., Cribb, M., Zhang, F., Yang, X., Zhao, C., Takemura, T., Wang, K., Xia, X., Yin, Y., Zhang, H., Guo, J., Zhai, P.M., Sugimoto, N., Babu, S.S., Rasseur, G.P., 2016. Aerosol and monsoon climate interactions over Asia: Aerosol and Monsoon climate Interactions. Rev. Geophys. 54 (4), 866–929. https://doi.org/10.1002/2015RG000500.

Li, Z., Guo, J., Ding, A., Liao, H., Liu, J., Sun, Y., Wang, T., Xue, H., Zhang, H., Zhu, B., 2017. Aerosol and boundary-layer interactions and impact on air quality. Nat. Sci. Rev. 4 (6), 810–833. https://doi.org/10.1093/nsr/nwx117.

Liu, Y., Shupe, M.D., Wang, Z., Mace, G., 2017. Cloud vertical distribution from combined surface and space radar-lidar observations at two Arctic atmospheric observatories. Atmos. Chem. Phys. 17, 5973–5989. https://doi.org/10.5194/acp-17-5973-2017.

Lompar, M., Ćurić, M., Romanić, D., 2017. Simulation of a severe convective storm using a numerical model with explicitly incorporated aerosols. Atmos. Res. 2017 (194), 164–177. https://doi.org/10.1016/j.atmosres.2017.04.037.

Lompar, M., Ćurić, M., Romanić, D., 2018. Implementation of a gust front head collapse scheme in the WRF numerical model. Atmos. Res. 2018 (203), 231–245. https://doi.org/10.1016/j.atmosres.2017.12.018.

Luo, Y.L., Zhang, R.H., Wang, H., 2009. Comparing occurrences and vertical structures of hydrometeors between eastern china and the Indian Monsoon Region using CloudSat/CALIPSO Data. J. Clim. 22 (4), 1052–1064. https://doi.org/10.1175/2008JCLI2606.1.

Mao, F., Duan, M., Min, Q., Gong, W., Pan, Z., Liu, G., 2015. Investigating the impact of haze on MODIS cloud detection. J. Geophys. Res. Atmos. 120. https://doi.org/10.1002/2015JD023555.

Martucci, G., Milroy, C., O'Dowd, C.D., 2010. Detection of cloud-base height using Jenoptik CHM15K and Vaisala CL31 ceilometers. J. Atmos. Ocean. Technol. 27, 305–318. https://doi.org/10.1175/2009JTECHA1326.1.

McGill, M., Hlavka, D., Hart, W., Scott, V.S., Spinhirne, J., Schmid, B., 2002. Cloud physics lidar: Instrument description and initial measurement results. Appl. Opt. 41 (18), 3725–3734. https://doi.org/10.1364/AO.41.003725.

Min, M., Wu, C., Li, C., Liu, H., Xu, N., Wu, X., Chen, L., Wang, F., Sun, F., Qin, D., Wang, X., Li, B., Zheng, Z., Cao, G., Dong, L., 2017. Developing the science product algorithm testbed for Chinese next-generation geostationary meteorological satellites: FengYun-4 series. J. Meteorol. Res. 31 (4), 708–719. https://doi.org/10.1007/s13351-017-6161-z.

Moran, K.P., Martner, B.E., Post, M.J., Kropfli, R.A., Welsh, D.C., Widener, K.B., 1998. An unattended cloud-profiling radar for use in climate research. Bull. Am. Meteorol. Soc.

79, 443–455. https://doi.org/10.1175/1520-0477(1998)079 < 0443:AUCPRF > 2.0. CO;2.

Mote, T.L., Lacke, M.C., Shepherd, J.M., 2007. Radar signatures of the urban effect on precipitation distribution: a case study for Atlanta, Georgia. Geophys. Res. Lett. 34, L20710. https://doi.org/10.1029/2007GL031903.

Narendra Reddy, N., Venkat Ratnam, M., Basha, G., Ravikiran, V., 2018. Cloud vertical structure over a tropical station obtained using long-term high-resolution Radiosonde measurements. Atmos. Chem. Phys. 18, 11709–11727. https://doi.org/10.5194/acp-18-11709-2018.

Oh, S.B., Kim, Y.H., Kim, K.H., Cho, C.H., Lim, E., 2016. Verification and correction of cloud base and top height retrievals from Ka–band cloud radar in Boseong, Korea. Adv. Atmos. Sci. 33, 73–84. https://doi.org/10.1007/s00376-0155058-y.

Poore, K.D., Wang, J.H., Rossow, W.B., 1995. Cloud layer thicknesses from a combination of surface and upper-air observations. J. Clim. 8, 550–568. https://doi.org/10.1175/1520-0442(1995)008 < 0550:CLTFAC > 2.0.CO;2.

Shang, H.Z., Letu, H., Nakajima, Y., Wang, Z., Ma, R., Wang, T., Lei, Y., Ji, D., Li, S., Shi, J., 2018. Diurnal cycle of cloud variations over Tibetan Plateau using Himawari-8. Sci. Rep. 8 (1), 1105. https://doi.org/10.1038/s41598-018-19431-w.

Stephens, G.L., 2005. Cloud feedbacks in the climate system: a critical review. J. Clim. 18, 237–273. https://doi.org/10.1175/JCLI-3243.1.

Sun, B.M., Karl, T.R., Seidel, D.J., 2007. Changes in cloud-ceiling heights and frequencies over the United States since the early 1950s. J. Clim. 20, 3956–3970. https://doi.org/10.1175/JCLI4213.1.

Wang, J.H., Rossow, W.B., 1995. Determination of cloud vertical structure from upper-air observations. J. Appl. Meteorol. 34, 2243–2258. https://doi.org/10.1175/1520-0450(1995)0342.0.CO;2.

Wang, S., Han, Z., Yao, Z., Zhao, Z., 2011. An analysis of cloud types and macroscopic characteristics over China and its neighborhood based on the CloudSat data. Acta Meteorol. Sin. 69 (5), 883–899.

Wang, F., Guo, J., Zhang, J., Huang, J., Min, M., Chen, T., Liu, H., Deng, M., Li, X., 2015. Multi-sensor quantification of aerosol-induced variability in warm cloud properties over eastern China. Atmos. Environ. 113, 1–9. https://doi.org/10.1016/j.atmosenv.2015.04.063.

Wang, Y., Zhao, C., Dong, Z., Li, Z., Hu, S., Chen, T., Tao, F., Wang, Y., 2018a. Improved retrieval of cloud base heights from ceilometer using a non-standard instrument method. Atmos. Res. 202, 148–155. https://doi.org/10.1016/j.atmosres.2017.11.021.

Wang, Z., Wang, Z.H., Cao, X.Z., Tao, F., 2018b. Comparison of cloud top heights derived from FY-2 meteorological satellites with heights derived from ground-based milli-meter wavelength cloud radar. Atmos. Res. 199, 113–127. https://doi.org/10.1016/j.atmosres.2017.09.009.

Webster, P.J., Stephens, G.L., 1984. Cloud-radiation interaction and the climate problem. In: Houghton, J. (Ed.), The Global Climate. Cambridge University Press, pp. 63–78.

Wild, M., 2012. New directions: a facelift for the picture of the global energy balance.

Atmos. Environ. 55, 366–367. https://doi.org/10.1016/j.atmosenv.2012.03.022.

Williams, A.P., Schwartz, R.E., Iacobellis, S., Seager, R., Cook, B.I., Still, C.J., Husak, G., Michaelsen, J., 2015. Urbanization causes increased cloud base height and decreased fog in coastal Southern California. Geophys. Res. Lett. 42. https://doi.org/10.1002/2015GL063266.

Xu, W., Zipser, E.J., Liu, C., 2009. Rainfall characteristics and convective properties of Mei-Yu precipitation systems over South China, Taiwan, and the South China Sea. Part I: TRMM observations. Mon. Weather Rev. 137 (12), 4261–4275.

Yang, Y.J., Lu, D.R., Fu, Y.F., Chen, F.J., Wang, Y., 2015. Spectral characteristics of Tropical Anvils obtained by combining TRMM Precipitation Radar with visible and infrared scanner data. Pure Appl. Geophys. 172 (6), 1717–1733. https://doi.org/10.1007/s00024-014-0965-x.

Yin, J.F., Wang, D.H., Zhai, G.Q., Wang, Z.E., 2013. Observational Characteristics of Cloud Vertical Profiles over the continent of East Asia from the CloudSat Data. J. Meteorol. Res. 27 (1), 26–39. https://doi.org/10.1007/s13351-013-0104-0.

Yin, J.F., Wang, D.H., Xu, H.B., Zhai, G.Q., 2015. An investigation into the three-di-mensional cloud structure over East Asia from the CALIPSO-GOCCP Data. Sci. China Earth Sci. 58 (12), 2236–2248. https://doi.org/10.1007/s11430-015-5205-4.

Yuter, S.E., Houze Jr., R.A., 1995a. Three-dimensional kinematic and microphysical evolution of Florida cumulonimbus. Part II: frequency distributions of vertical velo-city, reflectivity, and differential reflectivity. Mon. Weather Rev. 123, 1941–1963.

Yuter, S.E., Houze Jr., R.A., 1995b. Three-dimensional kinematic and microphysical evolution of Florida cumulonimbus. Part I: spatial distribution of updrafts, down-drafts, and precipitation. Mon. Weather Rev. 123, 1921–1940.

Zhang, C.Z., Uyeda, H., Yamada, H., Geng, B., Ni, Y.Q., 2006. Characteristics of mesoscale convective systems over the east part of continental China during the Meiyu from 2001 to 2003. J. Meteorol. Soc. Jpn. 84 (4), 763–782.

Zhang, W., Guo, J., Miao, Y., Liu, H., Li, Z., Zhai, P., 2016. Planetary boundary layer height from CALIOP compared to radiosonde over China. Atmos. Chem. Phys. 16, 9951–9963. https://doi.org/10.5194/acp-2016-250.

Zhang, W., Guo, J., Miao, Y., Liu, H., Song, Y., Fang, Z., He, J., Lou, M., Yan, Y., Li, Y., Zhai, P., 2018a. On the summertime planetary boundary layer with different ther-modynamic stability in China: a radiosonde perspective. J. Clim. 31 (4), 1451–1465. https://doi.org/10.1175/JCLI-D-17-0231.1.

Zhang, Y., Zhang, L., Guo, J., Feng, J., Cao, L., Wang, Y., Zhou, Q., Li, L., Li, B., Xu, H., Liu, L., An, N., Liu, H., 2018b. Climatology of cloud-base height from long-term radiosonde measurements in China. Adv. Atmos. Sci. 35 (2), 158–168. https://doi.org/10.1007/s00376-017-7096-0.

Zhao, C.F., Liu, L.P., Wang, Q.Q., Qiu, Y.M., Wang, Y., Wu, X.L., 2017. MMCR-based characteristic properties of non-precipitating cloud liquid droplets at Naqu site over Tibetan Plateau in July 2014. Atmos. Res. 190, 68–76. https://doi.org/10.1016/j.atmosres.2017.02.002.

Zhou, C., Zelinka, M.D., Klein, S.A., 2016. Impact of decadal cloud variations on the Earth's energy budget. Nat. Geosci. 9, 871–874. https://doi.org/10.1038/NGEO2828.